Effect of Noninteracting Intercalants on Layer Exfoliation in Transition-Metal Dichalcogenides

Jamil Missaoui[*], Antonio Cammarata[†], Florian Belviso, and Tomas Polcar

Department of Control Engineering, Faculty of Electrical Engineering, Czech Technical University in Prague, Technicka 2, 16627 Prague 6, Czech Republic

The control of friction at the atomic scale is fundamental to optimize the exfoliation of layered materials. To this aim, we report a density-functional investigation of how intercalated molecules affect the nanoscale friction of van der Waals transition-metal dichalcogenides. We find that the molecule does not interact with the electronic density of the layers directly; nonetheless it determines the features of the valence band of the system. In particular, the valence-band width appears to be a promising parameter to correlate the electronic properties with the nanofrictional response; it then constitutes a guide for the automatic search of intercalation molecules suitable for layer exfoliation. The present outcomes also constitute a theoretical tool for future investigations of the effect that intercalated species have on the nanoscale friction in layered materials.

I. INTRODUCTION

The discovery of graphene [1] opened up a new area of research into low-dimensional materials. Since then, many inorganic graphene analogs, such as boron nitride, boro-carbonitrides, metal oxides, metal-organic frameworks, and transition-metal dichalcogenides (TMDs) [2,3] have attracted great attention because of their wide applicability in photovoltaic devices, lithium-ion batteries, hydrogen-evolution catalysis, transistors, photodetectors, DNA detection, memory devices, and tribological applications [4–7]. Among the compounds mentioned, we focus here on TMDs, lamellar structures held together by weak van der Waals forces.

Like graphene and other van der Waals solids, bulk TMDs can be exfoliated into single-layer or few-layer structures by physical or chemical routes, such as the adhesive tape technique [8], solvent-assisted exfoliation [9], and chemical exfoliation via ion intercalation [10–12]. Exfoliation of these materials into monolayer or few-layer thin films leads to additional exciting properties due to confinement effects, which are not seen in the bulk counterparts [13–18]. In this respect, great expectations are placed on finite two-dimensional systems, where transition-metal dichalcogenides play a fundamental role—the flexible chemistry and stoichiometry easily open several routes to engineer heterostructures with diverse functionalities at the nanoscale.

The fundamental starting point to build two-dimensional TMD-based systems is to obtain monolayer or few-layer TMD films. The crucial aspect involved in harnessing layer exfoliation is understanding the interlayer environment. In bulk TMD structures, the weak van der Waals forces allow relative sliding of adjacent layers and ease layer separation under external stimulations. Individual layers of TMDs can be isolated from the bulk parent via mechanical cleavage [19–21], liquid exfoliation [22,23], or ion intercalation [11,24–26]. Mechanical cleavage produces single-crystal flakes of high purity and cleanliness that are suitable for characterization and fabrication of individual devices. However, this method is not scalable yet, and does not allow systematic control of flake thickness and size [27]. A focused laser spot has been used to reduce MoS_2 bulk to monolayers by thermal ablation, but the requirement for laser scanning makes it challenging for scale-up [28]. On the other hand, liquid-phase exfoliation of TMDs is very promising. Sonication-assisted exfoliation in solvents [22,23,29,30] results in the production of single-layer and multilayer nanosheets that are then stabilized by interactions with the solvent and surfactant. This method has the advantage of being simple despite it producing high-quality small exfoliated nanosheets, but one of the main drawbacks is that very little is known about the stabilization mechanism [31]. Finally, ion intercalation has been regarded as an efficient way to reduce several layered compounds into thin sheets [32,33]; however, this method is time-consuming, is extremely sensitive to environmental conditions, and can result in structural deformations [34], besides the complication represented by ion removal and the subsequent reaggregation of layers

*missajam@fel.cvut.cz
†cammaant@fel.cvut.cz

[35]. The most-promising method would then seem to be the intercalation of inert species rather than ionic species to prevent unwanted interactions.

Computational investigations of exfoliation of layered materials have focused mainly on interlayer adhesion energies also in the presence of exfoliation-assisting molecules [36–40], and very few of them have dealt with TMD compounds [41]. Adhesion is the main force resisting the layer peeling, and is then one of the main structural responses to be harnessed to facilitate the exfoliation process. However, adhesion is inevitably accompanied by the resistance that adjacent atomic layers develop to prevent the relative parallel shift, this occurring because the exfoliation is initiated and done by mechanical stress at a tangent to the layer surface [42–45]: layer sliding and layer separation are the two main phenomena that must be controlled to obtain a facile exfoliation of the lamellar structure. Nanotribological properties of TMD layers therefore play a fundamental role in the exfoliation process.

Following the perspective outlined above, in the present work we focus on how inert molecules change the tribological properties of TMD layers when intercalated in the interlayer gap. The presence of the molecule induces an increase of the interlayer spacing and weakens the van der Waals interaction and hence the forces binding the layers together and preventing the layer sliding [44]; as a consequence, the layer gliding is favored, and the energy required to separate the layers is reduced. It has been shown [46] that intercalated water molecules in MoS_2 considerably hinder the sliding motion of the layer. Moreover, an enhancement of friction by water intercalation between graphene and mica by a factor of approximately 3 relative to dry mica was found [47]; this has been supported by density-functional-theory calculations that revealed that the water broadens the spectral range of graphene vibrations, leading to new excitation channels and increasing the overlap with the atomic vibrations of the mica substrate. We earlier observed that specific phonon modes play a fundamental role in energy transfer under tribological conditions in TMD-based materials [48]. In the present work, by means of quantum-mechanical simulations, we show that the nanotribological properties correlate with the modifications induced in the valence band of the pristine material. Although the molecule does not interact with the atoms of the TMD layer, we find that the electronic states of the molecule modify the relative M/X composition of the occupied states up to the Fermi level [49] together with the width of the valence band; the latter appears to be the quantity to control to tune the frictional response at the nanoscale in the presence of inert intercalated moieties. Finally, we discuss how the present outcomes could constitute a starting point to develop experimental guidelines for the selection of inert species to assist the exfoliation of layered materials, thus boosting the development of nanoengineered devices with wide applicability.

II. METHODS

A. Computational details

Pristine TMDs are layered structures, with the formula unit MX_2, where M is a transition metal and X is a chalcogen atom; M—X bonds are arranged in a trigonal prismatic configuration forming layers characterized by strong covalent character, which provides in-plane stability of the periodic structure; the layers are held together by weak out-of-plane van der Waals interactions, allowing easy relative sliding parallel to the layer planes. We select the hexagonal $P6_3/mmc$ 2H polymorphs [5] with M being Mo or W and X being S, Se, or Te as reference structures [50–55]. We also consider the presence of one CO_2 molecule or one N_2 molecule in the interlayer gap of a $2 \times 2 \times 1$ supercell of the pristine geometry. In this way, we build the model geometries for our simulations, which we name Z-MX, where M and X specify the kind of cation and anion forming the MX_2 layers, respectively, while Z (N_2 or CO_2) specifies the intercalated molecular species; $Z = 0$ indicates that no molecule is present in the unit cell and the structure is the pristine one (Fig. 1).

Our calculations are based on density-functional theory with projector-augmented-wave formalism for the specification of the atom pseudopotentials as implemented in the ABINIT package [56–59]. After preliminary benchmarks [60], we choose the Perdew-Burke-Ernzerhof energy functional [61] for the exchange-correlation potential and the DFT-D3(BJ) van der Waals correction [62] for the representation of the long-range interlayer interactions. We select a cutoff energy for the plane-wave basis set of 700 eV and sample the Brillouin zone by using a $7 \times 7 \times 5$ Monkhorst-Pack division [63]. The solution of the self-consistent-field equations is considered converged within an energy tolerance of 10^{-10} eV, while the atomic positions
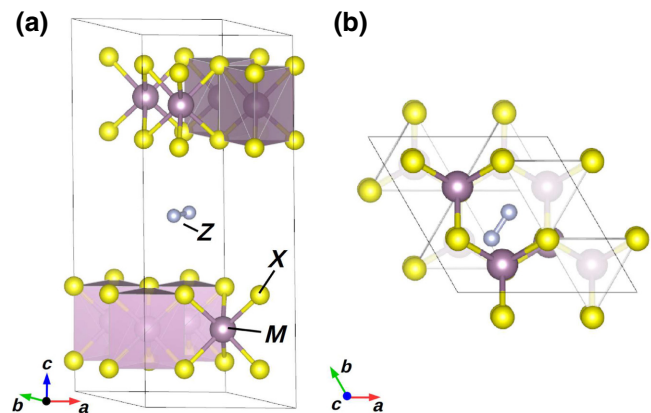

FIG. 1. Schematic of a Z-MX model geometry; here, $Z = N_2$ as an example. Each M cation coordinates six X anions via covalent bonds, forming MX_2 layers; the Z molecule sits in the interlayer gap and modulates the van der Waals forces binding the layers together. (a) Lateral view; (b) view along the c axis.

and lattice parameters are fully relaxed with a tolerance of 5×10^{-6} eV/Å. We perform several geometric optimizations that differ in the starting position and orientation of the molecule. Despite the differences among the starting geometries, the corresponding final optimized configurations are identical within a tolerance of 10^{-4} Å; we then consider the ground-state geometries obtained to be well defined and we consider these in the present calculations. The stable geometries containing the intercalant molecule are reported in Supplemental Material [64].

We use PHONOPY [65] to diagonalize the dynamical matrix of the stable structures built with the finite-displacement method [66,67], whereas the force constants are evaluated on $2 \times 2 \times 2$ and $1 \times 1 \times 2$ supercells of the pristine and molecule-containing systems, respectively.

B. Sliding and breathing modes

The exfoliation process occurs because of the combined action of external forces acting along the shear and vertical directions with respect to the layer plane [42–45]; such forces are capable of overcoming the internal forces that bind the layers together. This can be visualized in the following way. If an external macroscopic force acts on the system with a non-null component at a tangent to the material surface, the atomic layers slide on shearing. As a response, internal forces opposing the shift develop, and the relative motion is realized as long as the external tangent force is active and larger than the internal forces. The internal forces manifest themselves as friction and are the result of several factors, such as asperities, dislocations, layer truncations, and defects; if such irregularities are not present, friction still occurs and is due to only the interatomic forces arising from the electronic density and the atomic geometry. In this latter case, we refer to it as "intrinsic friction" since it is an intrinsic characteristic of the system [60,68,69], and it is the subject of the present study.

Relative atomic motions are usually described by a set of Cartesian vectors, the components of which represent the atomic displacements. An equivalent description is obtained by using suitable linear combinations of phonon eigendisplacements, which are a complete geometric basis set and therefore provide complete information on the atomic configuration [70–72]. The phonon eigenvectors representing relative layer displacemements parallel to the layer planes are named "sliding modes" [73,74]: they appear with the largest coefficients in the linear combination and keep active the layer sliding as long as their population is above a certain threshold [48,75]. The sliding modes may be visualized as restoring forces that return the layers to their equilibrium position; in the harmonic approximation, they are proportional to the square of the mode frequency. As a consequence, a low frequency associated with the sliding modes corresponds to a low restoring frictional force and hence to low intrinsic friction and facile sliding.

In addition to parallel sliding, other kinds of displacements are significant during the exfoliation process. The lateral displacement of the layers generates an excessive overlap of the atomic electronic densities in the interlayer gap; as a consequence, a repulsive force arises due to Coulombic interaction and the Pauli exclusion principle. As the effect of the external force is to drag the layers along directions parallel to the MX_2 planes, such repulsive force results into an increased separation of the layers; if this movement were not allowed, then the repulsive force would push the layers laterally back, thus increasing the sliding energy barrier. This means that if the forces tying the layers together are weak, then it is easier to separate them, and the sliding is promoted. These forces arise mainly from the van der Waals interactions and manifest themselves as the *breathing* phonon modes; they may be regarded as the harmonic representation of adhesion forces. Analogously to the sliding modes, a low breathing frequency then corresponds to an easy variation of the interlayer distance and hence to low adhesion and facilitated sliding.

Both sliding and breathing modes are then active whenever two subsequent layers are laterally displaced to be separated; if the separation occurs because of only vertical forces, then solely the breathing modes are active and hinder the exfoliation. The control of both sliding and breathing frequencies is then desirable to optimize the exfoliation process. To this aim, we focus on the frequencies of both the sliding modes and the breathing modes. To reduce the number of parameters and facilitate the analysis, we consider the mean sliding frequency ω_{sl}, which reads

$$\omega_{\text{sl}} = \frac{1}{N} \sum_{j}^{N} \omega_j, \tag{1}$$

where ω_j is the frequency of the jth sliding mode and N is the total number of sliding modes considered; the mean breathing frequency ω_{br} is defined in an analogous way. In practice, the distinction between breathing modes and sliding modes is done by considering reference vectors parallel and perpendicular to the layer surface. The modes with large scalar projections along the parallel or perpendicular reference vectors are labeled as sliding modes and breathing modes, respectively. This characterization criterion has already been used for the mode decomposition of sliding trajectories [75].

III. RESULTS AND DISCUSSION

We begin our analysis by considering the features of the unit cell. As soon as a molecule is inserted into the interlayer region, the symmetries of the pristine structure are

reduced to those of the $P1$ crystallographic space group. For fixed M and X atomic species, lattice parameters a and b are not affected by the kind of molecule, while the main variation is observed for the c crystallographic axis, which accounts for the volume increase (Fig. 2); no significant difference is found instead for the cases with the two different molecules. In general, the presence of a molecule induces a lowering of ω_{sl} and ω_{br} with respect to the pristine case ($Z = 0$), irrespective of the chemical composition of the layers; this is expected, because the presence of the molecule increases the separation between the layers and screens the interaction between them, making the sliding (friction) and breathing (adhesion) restoring forces weaker. However, although the steric hindrance of the CO_2 molecule is larger than that of N_2 molecule, the effect on the mean sliding and breathing frequencies is a peculiarity of the system (Fig. 3): while the mean sliding frequency decreases in the sequence $0 > N_2 > CO_2$, the mean breathing frequency increases in the Z-MoS, Z-MoSe, and Z-WTe systems when Z changes from N_2 to CO_2. A comparison between Figs. 2 and 3 shows that

FIG. 3.   Average frequency of (a) sliding modes and (b) breathing modes for the molecular moieties considered. The legend is common to both plots.

there is no direct relation between the cell volume and the frequency shift; ω_{sl} and ω_{br} increase or decrease with the volume according to the specific chemical composition (Fig. 4). The frequency shift is not then a mere result of the change in the geometry of the system but arises from the subtle interplay between the electronic features and the dynamic features. The phonon frequencies are obtained from the diagonalization of the dynamical matrix, which, in turn, is the normalized Fourier transform of the interatomic force constants [70,71]; these depend on the atomic types forming the system and determining the electronic environment in which they are embedded. Any change induced in the electronic distribution of the pristine material is therefore reflected in a change of the
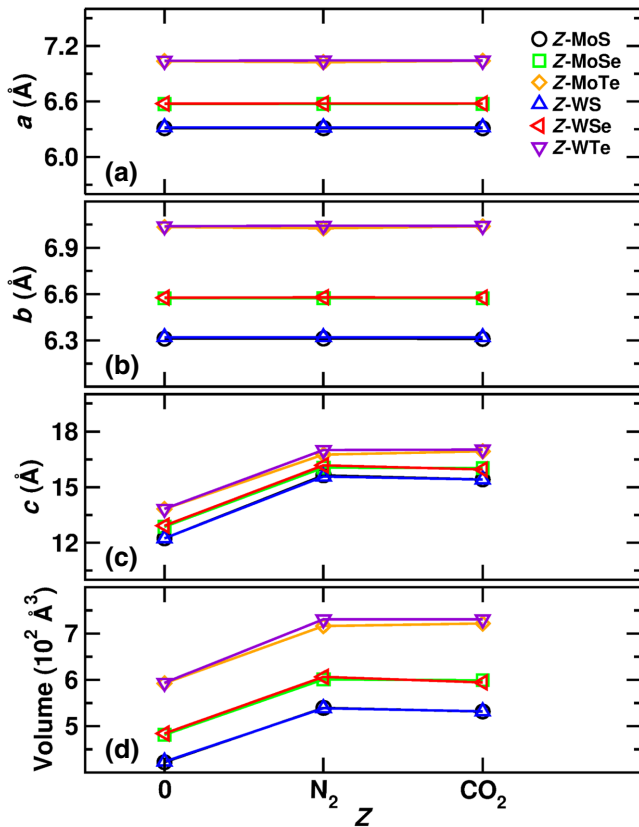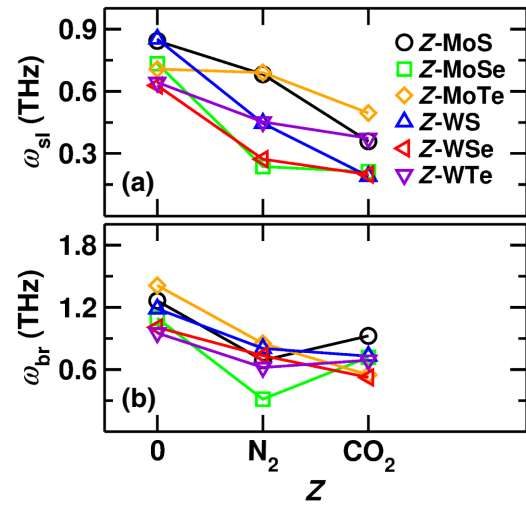

FIG. 2.   (a)–(c) Length of the lattice vectors and (d) volume of the unit cell of the systems considered for different molecular moieties in the interlayer gap. The legend is common to all plots. For a fixed Z, the values relative to systems with the same X anion are very close and the corresponding data points almost overlap in all the plots.
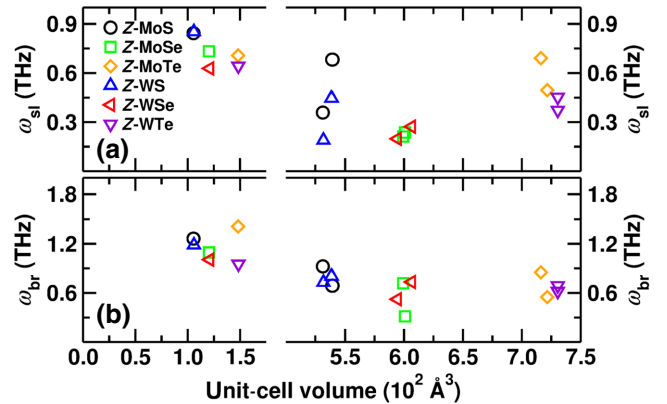

FIG. 4.   Average frequency of (a) sliding modes and (b) breathing modes as a function of the unit-cell volume. Volumes in the left part of the plots correspond to the 0-MX systems. The legend is common to both plots.
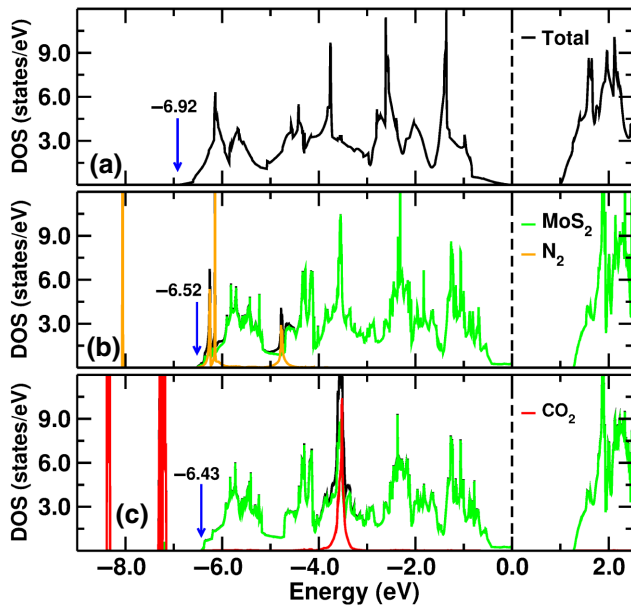
FIG. 5. Density of states of the (a) 0-MoS, (b) N_2-MoS, and (c) CO_2-MoS systems. The DOS are normalized by a factor chosen to optimize the visualization. In each plot, the Fermi level is set to 0 eV and is marked by a vertical dashed line, while the blue arrow indicates the position of the bottom of the valence band, with the corresponding value reported immediately above. The legends are common to the different plots as appropriate.

atomic interactions and the corresponding phonon frequencies. For this reason, we continue our analysis by focusing on the electronic density of states (DOS).

A typical profile of Z-MX electronic DOS is reported in Fig. 5, where we show the case of the Z-MoS systems.

The valence band of the pristine material covers the energy range from -6.92 to 0 eV [Fig. 5(a)]; once a molecule is inserted into the interlayer gap, the width of the valence band is narrowed by an amount that depends on the kind of molecule [Figs. 5(b) and 5(c)]. The atom-projected DOS reveals that the molecule contributes with its own states to the valence band; however, no hybridization occurs between the atomiclike wave functions centered at the molecule and those centered at each surrounding X anion. This behavior is expected because N_2 and CO_2 are inert gases and any non-null wave-function overlap would indicate an interaction between the molecule and the layers. This is apparent from the analysis of the partial electronic density generated by our considering the energy bands relative to the range that includes the Z states in the valence band (Fig. 6): the partial electronic distribution is localized on the molecule and around the cation within the layer, while no density shared between the layers and the molecule is found. The effect of the orbitals of the molecule is then to change the width of the valence band by contributing to the wave function of the whole system without interacting with the orbitals of MX_2 layer, but yet determining the relative position of the latter within the valence band. By comparing Figs. 2 and 7(a), we see that the valence-band width does not correlate with the length of the lattice vectors nor with the system volume; interestingly, the width decreases in the sequence $0 > N_2 > CO_2$ irrespective of the chemical composition of the layers. Such behavior is similar to that found for the sliding and breathing frequencies (Fig. 3); ω_{sl} and ω_{br} seem to correlate with the width of the valence band [Figs. 7(b) and 7(c)]. In general, we observe that an increase of the valence-band width favors higher sliding and breathing frequencies; this
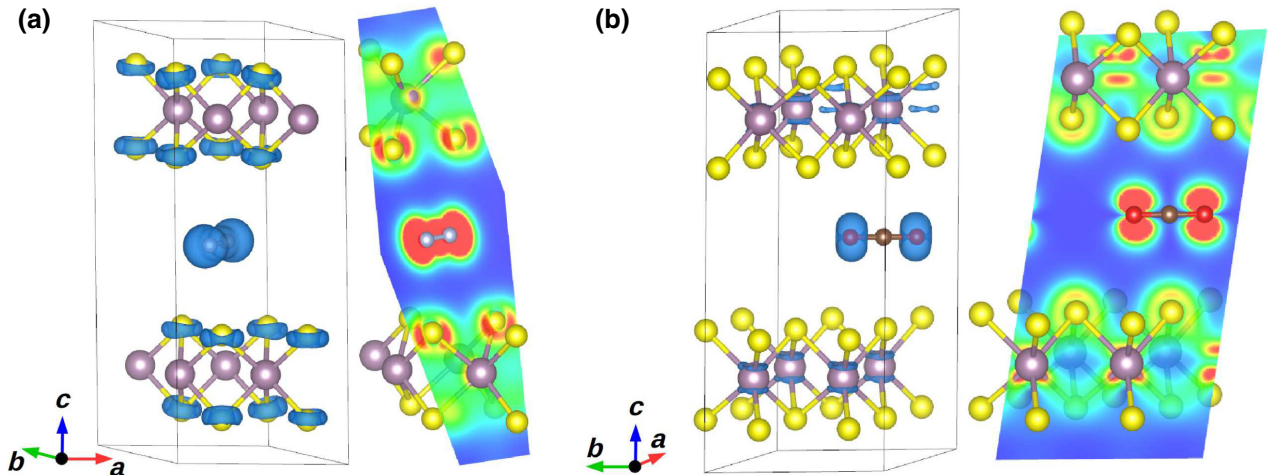

FIG. 6. Isosurface (blue) and plane projection of the partial charge density in (a) N_2-MoS and (b) CO_2-MoS obtained by our selecting the electronic bands in the range $[-6.5, -6.0] \cup [-5.0, -4.5]$ and $[-4.0, -3.2]$ eV, respectively, each including the corresponding Z states (see Fig. 5). No significant charge is found in the region between the molecule and the sulfur atoms, this showing that no hybridization occurs between the S-centered and molecule-centered atomic orbitals. The red-green-blue color gradient indicates decreasing charge density.
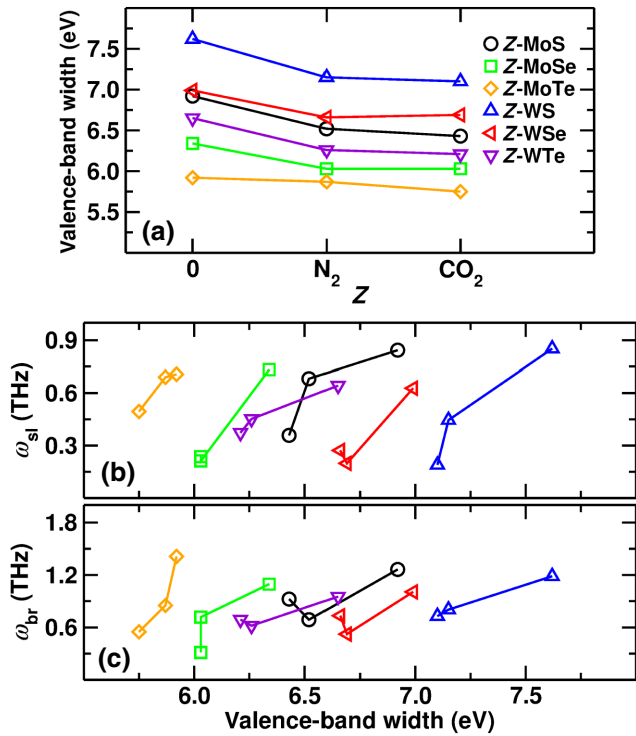
FIG. 7. (a) Width of the valence band as a function of the inter-calated moiety. Average frequency of (b) sliding modes and (c) breathing modes as a function of the width of the valence band. The legend is common to all plots.

FIG. 8. (a) M—X bond covalency as a function of the molecular moiety. (b),(c) The average frequencies of the sliding modes and the breathing modes do not seem to correlate with the bond covalency as they increase or decrease with $C_{M,X}$ in a different way for different chemical compositions. The legend is common to all plots.

suggests that it is beneficial to narrow the valence band to reduce the lateral friction and the layer adhesion and hence to promote the layer exfoliation. In passing, we note that the variation range of the valence-band width depends on the specific atomic type forming the layers; for practical applications, it can be pre-evaluated in high-throughput calculations before the experimental validation of the selected exfoliation-assisting species. As shown above, although the orbitals of molecule are involved in the formation of the valence band, they do not interact with the atomlike orbitals pertaining to the M and X ions; however, the modification of the width of the valence band affects the relative position of the M and X orbitals. This has the effect of modulating the overlap of the M and X atom-projected wave functions generating the interatomic charge density and hence of determining the covalent character of the M—X bond. To quantify this effect, we calculate the covalency $C_{M,X}$ of the M—X bonds in terms of the M and X atomic contributions to the DOS in the valence band. The mathematical formulation of $C_{M,X}$ can be found, for example, in Ref. [76]; the integrals appearing in the formulation are evaluated in the range $[-w, 0]$, where w is the width of the valence band reported in Fig. 7. No clear behavior is found for $C_{M,X}$ as a function of Z [Fig. 8(a)]. While, for instance, a change of the Z species induces a variation of the covalency in the
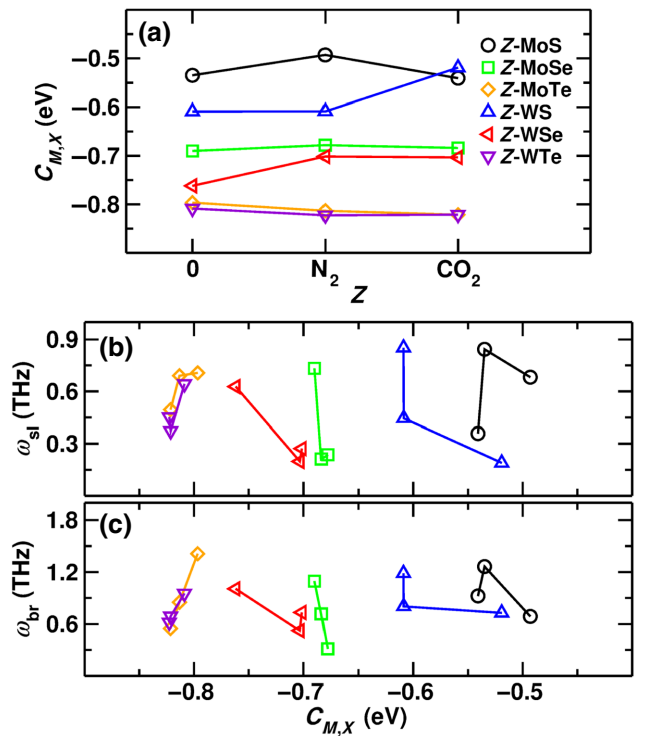
Z-WS and Z-WSe systems, no significant change occurs for the remaining systems. Correspondingly, no correlation is found between ω_{sl} or ω_{br} and $C_{M,X}$ [Figs. 8(b) and 8(c)], as the mean frequencies increase or decrease according to the atomic types forming the system. Incidentally, the ordering of the covalent character for $Z = 0$ is consistent with what we reported in Ref. [73], where different a van der Waals correction, energy cutoff and k-mesh sampling were used. To investigate the subtle variation in the electronic density induced by the Z species, we consider the orbital polarization [60,77,78] $\mathcal{P}_{a,b}$ defined as

$$\mathcal{P}_{j,k} = \frac{n_j - n_k}{n_j + n_k}, \quad (2)$$

where j and k are two sets of atomic orbitals, while n_j and n_k are their respective occupations. With this definition, $\mathcal{P}_{j,k}$ measures the excess of charge in the j orbital with respect to the k orbital. We choose atom-centered hydrogenlike orbitals to calculate the orbital polarizations $\mathcal{P}_{p_x,p_y}$, $\mathcal{P}_{p_x,p_z}$, and $\mathcal{P}_{p_y,p_z}$ of the X atoms, and $\mathcal{P}_{t_{2g},e_g}$ and $\mathcal{P}_{d_{x^2-y^2},d_{z^2}}$ of the M cations; in this way, we are able to partition the space according to the directional character of the orbital and to monitor possible preferential distributions of the
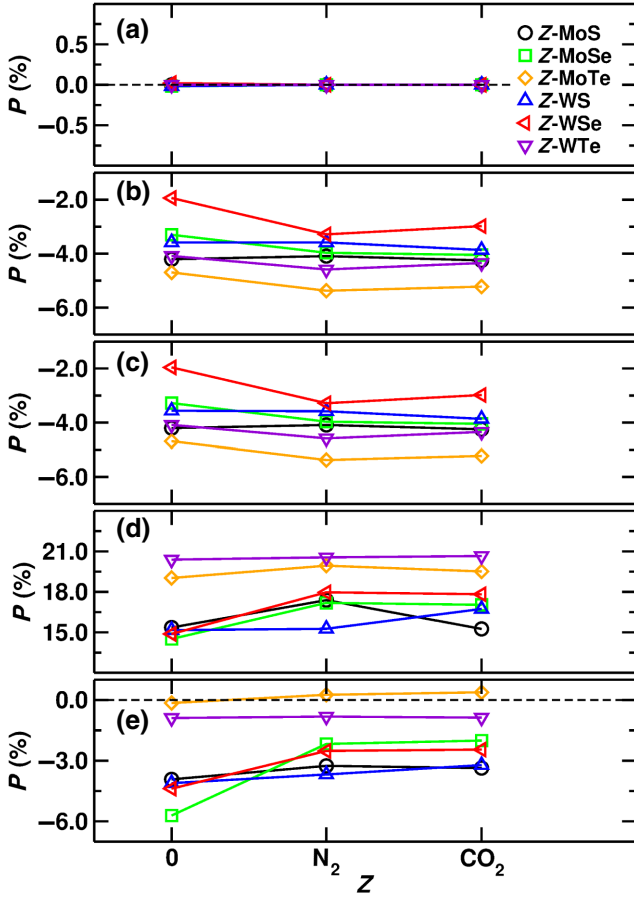
FIG. 9. Orbital polarization of the Z-MX systems versus the intercalated moiety: (a) X $\mathcal{P}_{p_x,p_y}$, (b) X $\mathcal{P}_{p_x,p_z}$, (c) X $\mathcal{P}_{p_y,p_z}$, (d) M $\mathcal{P}_{t_{2g},e_g}$, and (e) M $\mathcal{P}_{d_{x^2-y^2},d_{z^2}}$. Lines are a guide for the eye.

charge density for different M, X, and Z species. We first observe that, irrespective of the chemical composition, the p_x and p_y orbitals of the X anion are equally populated [Fig. 9(a)]; this is consistent with the fact that the kind of molecule does not affect lattice parameters a and b [Figs. 2(a) and 2(b)], while the equivalence between the a and b crystallographic axes is preserved within the MX_2 layers, such equivalence being present in the pristine system. The change in lattice parameter c with Z [Fig. 2(c)] is instead reflected in $\mathcal{P}_{p_x,p_z}$ and $\mathcal{P}_{p_y,p_z}$ [Figs. 9(b) and 9(c)]: while negative values indicate an excess of electrons at the X site along an axis orthogonal to the layer planes, the presence of a molecule induces, in general, a further accumulation along the same direction. The in-layer local equivalence between the a and b crystallographic axes is reflected in the fact that, for each Z-MX configuration, identical $\mathcal{P}_{p_x,p_z}$ and $\mathcal{P}_{p_y,p_z}$ values are realized. The positive values of $\mathcal{P}_{t_{2g},e_g}$ indicate that an excess of electrons is found in the t_{2g} orbitals, thus favoring an in-plane distribution of the charge [Fig. 9(d)] irrespective of Z; such a distribution is altered in a different way according to

the kind of molecule and by a different amount specific to the atomic types forming the layers. The largest variation is found for the Z-MoSe and Z-WSe systems, in a way similar to that observed for $\mathcal{P}_{d_{x^2-y^2},d_{z^2}}$. The negative values of the latter point to a preferential distribution of the d_{z^2} orbital with respect to the $d_{x^2-y^2}$ orbital [Fig. 9(e)]; however, a comparison with $\mathcal{P}_{t_{2g},e_g}$ excludes charge accumulation along an axis perpendicular to the layer planes. This analysis shows that there is no clear connection between the Z species and the charge arrangement within the layer; accordingly, no clear relation is found between the orbital polarizations and the sliding and breathing frequencies. This result is different from what we found in the pristine MX_2 systems under different stimuli, in which the orbital polarization plays instead a fundamental role in determining the nanoscale frictional behavior [60,69,79]. We conclude that the molecule suppresses the effect of the details of the electronic distribution inside the layer on the vibrational modes considered. In our analysis so far, we used the properties of the equilibrium geometry to estimate the response of the system during the layer sliding and separation (i.e., to predict the system behavior far from equilibrium). We now want to check the reliability of such a prediction. As a first step, for each of the systems considered, we create a *sliding path* along the M—X bond [Fig. 10(a)]. A sliding path is a sequence of configurations (atom positions and lattice parameters) that represent the relative parallel shift of two subsequent MX_2 layers. The initial guess of the paths is obtained by our considering linear combinations of eigenvectors corresponding to the sliding modes, according to the prescription of the *normal-modes transition approximation* [74]; in this way, we create a total of 11 configurations for each sliding path. We then perform a climbing-image nudged-elastic-band (CI NEB) [80,81] full relaxation (atom positions and lattice vectors) of the paths by means of the software program VASP [82,83]; the general parameters (e.g., mesh sampling, energy cutoff, and tolerances) are the same as those presented in Sec. II A. As a result of the climbing-image NEB calculations, we obtain the potential energy barrier ΔE_{bar} associated with the relative layer sliding. We can then define the average friction force f_{fr} as

$$f_{\text{fr}} = \frac{\Delta E_{\text{bar}}}{\Delta R_{\text{NEB}}}, \qquad (3)$$

where ΔE_{bar} is the difference between the energy of the ground state and the maximum energy realized along the path, while

$$\Delta R_{\text{NEB}} = \sqrt{\sum_{i=1}^{N} \left| \mathbf{R}_{\text{bar}}^{i} - \mathbf{R}_{0}^{i} \right|}, \qquad (4)$$

with $\mathbf{R}_{\text{bar}}^{i}$ being the position of the ith atom in the configuration realizing the energy maximum and $\mathbf{R}_{0}^{i}$ being the
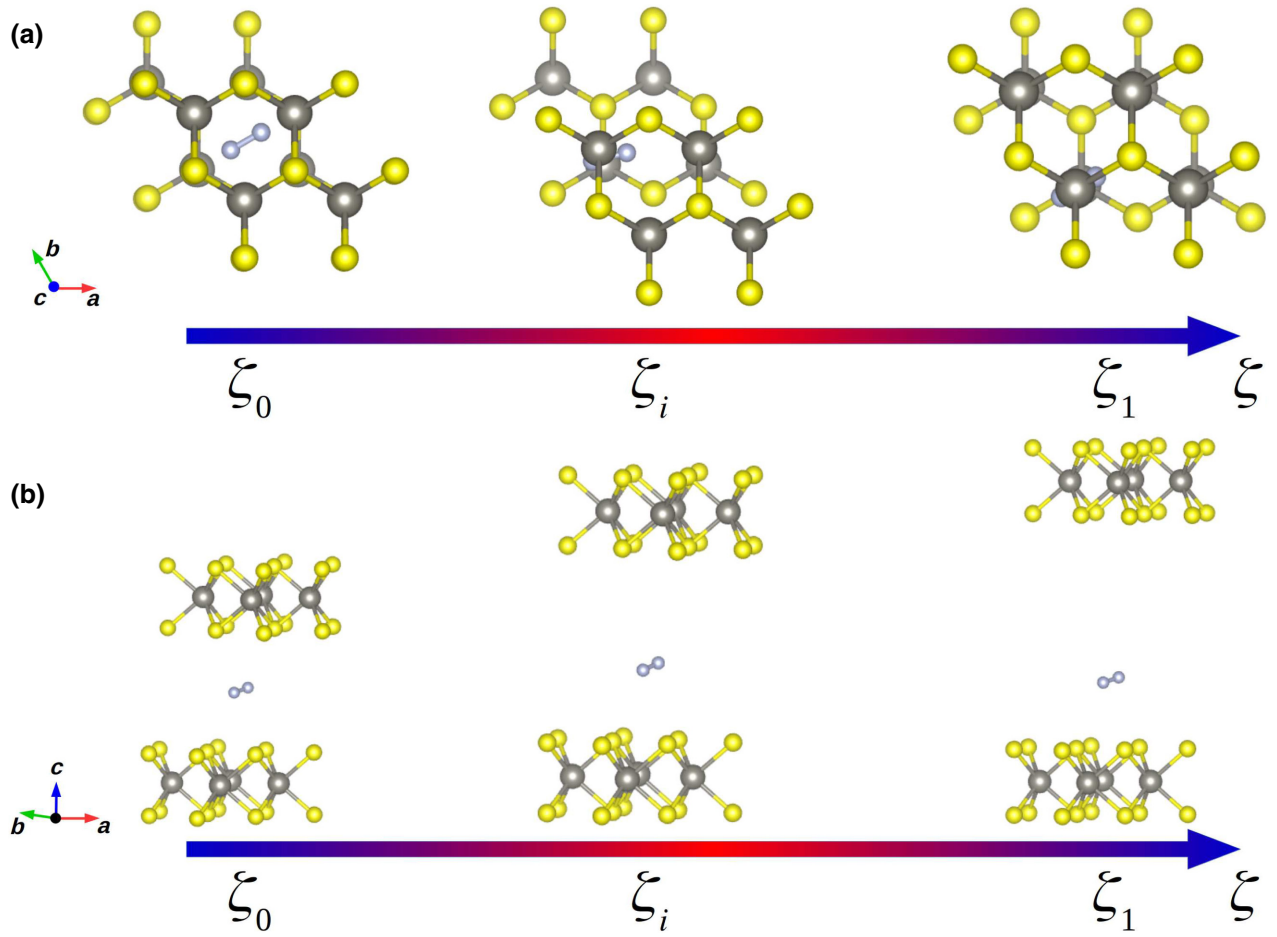
FIG. 10. Example of (a) sliding path and (b) layer separation. Along the configurational coordinate ζ, the initial state, an intermediate state, and the final state are indicated with ζ_0, ζ_i, and ζ_1, respectively.

position of the same atom in the equilibrium geometry. With this definition, ΔR_{NEB} is a measure of the displacement covered by the atoms during the sliding. As a second step, we estimate the adhesion force. Starting from the equilibrium geometry, we consider 11 geometric configurations in which the two layers are progressively shifted along the c-axis direction until the interlayer distance is approximately 15Å [Fig. 10(b)]. For each configuration, we fix the lattice parameters and the positions of the M cations, and finally optimize the coordinates of the remaining atoms. By tracking the evolution of the system energy as a function of the interlayer distance, we observe an asymptotic behavior; this assures us that the last configuration corresponds to noninteracting (separated) layers. Analogously to the definition of the average friction force f_{fr} [Eq. (3)], we then define the average adhesion force f_{ad} as

$$f_{\mathrm{ad}} = \frac{\Delta E_{\mathrm{sep}}}{\Delta R_{\mathrm{sep}}}, \tag{5}$$

where ΔE_{sep} is the difference between the energy of the ground state and the energy of last configuration, while ΔR_{sep} is the layer-layer distance. Similarly to what we observe for the sliding-mode and breathing-mode frequencies, the frictional and adhesion forces display large values in correspondence with large values of the band width (Fig. 11). Moreover, we notice that the adhesion forces are larger than the frictional forces, as the breathing frequencies are larger than the sliding frequencies; this supports the harmonic representation of the two forces discussed in Sec. II B. In the same section, we examined how both lateral friction and adhesion forces appear during the exfoliation process. This suggests we consider an average force $f_{\mathrm{av}} = (f_{\mathrm{fr}} + f_{\mathrm{ad}})/2$ arising during the exfoliation; analogously, we consider the average frequency $\omega_{\mathrm{av}} = (\omega_{\mathrm{sl}} + \omega_{\mathrm{br}})/2$. In general, we notice that both quantities increase with increasing valence-band width (Fig. 12). These results suggest that from the analysis of the equilibrium geometry (electronic structure, phonon spectrum) we may infer the response of the system far from equilibrium (layer sliding and separation); in this respect, the width of the valence
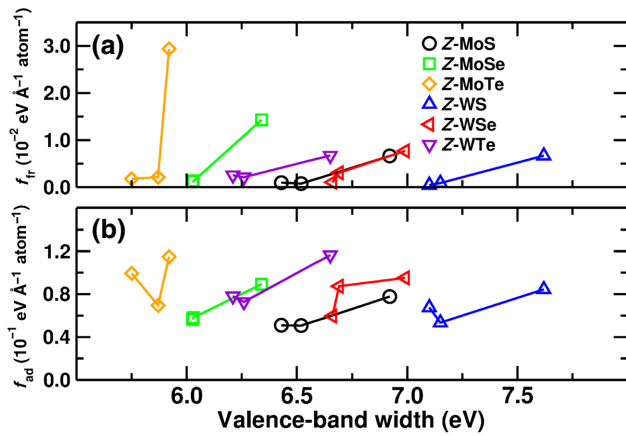
FIG. 11. (a) Lateral frictional force and (b) adhesion force as a function of the width of the valence band. The legend is common to both plots.

band seems to be a useful descriptor to parametrize the forces opposing the layer exfoliation in the presence of inert intercalated molecules.

To further confirm these findings, more inert species and geometries should be the subject of future studies in which the analysis method presented here is applied. Unfortunately, the presence of a molecule reduces the symmetries of the systems to only the translation (space group $P1$). This implies the need to evaluate the ground-state wave function by using a very dense Brillouin-zone sampling, and the calculation of the atomic forces on many distorted configurations, to obtain the phonon spectrum. Moreover, the identification of the stable geometry requires the optimization of several starting configurations differing in the initial molecule position, thus increasing further the computational needs to consider more kinds of intercalant species. For this reason, we limit our analysis to the study
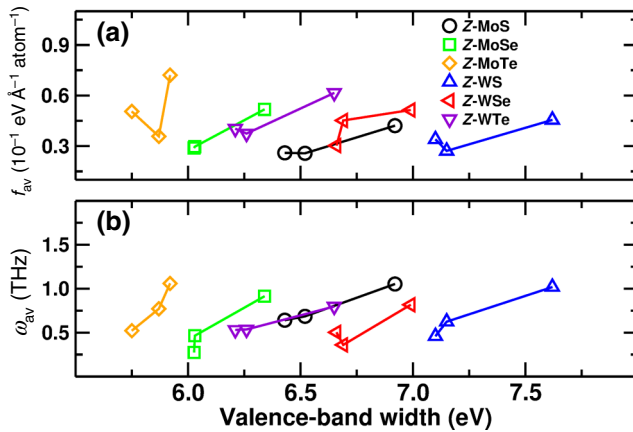

FIG. 12. (a) Average force and (b) average mode frequency as a function of the width of the valence band. Legend is common to all the subfigures.

cases presented. However, we believe that our results already point to an alternative route for how to investigate the relation between the electronic structure and the nanoscale mechanisms hindering the exfoliation. Finally, the width of the valence band seems to be a promising descriptor for automated engines aimed at screening databases in search of suitable exfoliation-assisting moieties, boosting the design of nanoengineered devices with targeted functionalities.

IV. CONCLUSIONS

We study how inert molecules modify the nanofrictional response when used as an intercalant for exfoliation in van der Waals transition-metal dichalcogenides. The exfoliation occurs if the applied external forces, aimed at separating the layers, are larger than the internal forces that return the atoms to their equilibrium positions; such internal forces manifest themselves as internal friction. If we are able to reduce the internal friction, we can facilitate the exfoliation process. We find that the inert intercalated molecule determines the width of the valence band although it does not interact with the atoms of the layers. The valence-band width seems to correlate with the vibrational properties related to the nanoscale friction: small widths correspond to small interlayer binding forces and hence to reduced friction and easy layer sliding and separation. A similar correlation is found with the friction and adhesion forces: the larger the valence-band width, the larger the forces. Since such forces arise during the exfoliation process, our results suggest that suitable values of the band width may ultimately assist the exfoliation. The analysis protocol presented can be used in systematic studies on the frictional response in the presence of inert intercalated species; this would help to define the potentiality and the limitations of the valence-band width as a friction descriptor. The present results also suggest suitable inert molecules to be used in combination with other methods directed at the fine control of the valence band, such as external electric fields [60].

[1] K. S. Novoselov, A. K. Geim, S. V. Morozov, D. Jiang, Y. Zhang, S. V. Dubonos, I. V. Grigorieva, and A. A. Firsov, Electric field effect in atomically thin carbon films, Science **306,** 666 (2004).

[2] Dmitri Golberg, Yoshio Bando, Yang Huang, Takeshi Terao, Masanori Mitome, Chengchun Tang, and Chunyi Zhi, Boron nitride nanotubes and nanosheets, ACS Nano **4,** 2979 (2010).

[3] C. N. R. Rao and Urmimala Maitra, Inorganic graphene analogs, Ann. Rev. Mater. Res. **45,** 29 (2015).

[4] Hai Li, Jumiati Wu, Zongyou Yin, and Hua Zhang, Preparation and applications of mechanically exfoliated single-layer and multilayer MoS_2 and WSe_2 nanosheets, Accounts Chem. Res. **47,** 1067 (2014).

[5] Manish Chhowalla, Hyeon Suk Shin, Goki Eda, Lain-Jong Li, Kian Ping Loh, and Hua Zhang, The chemistry of two-dimensional layered transition metal dichalcogenide nanosheets, Nat. Chem. **5,** 263 (2013).

[6] A. K. Geim and I. V. Grigorieva, Van der waals heterostructures, Nature **499,** 419 (2013), perspectives.

[7] Andrea Vanossi, Nicola Manini, Michael Urbakh, Stefano Zapperi, and Erio Tosatti, *Colloquium*: Modeling friction: From nanoscale to mesoscale, Rev. Mod. Phys. **85,** 529 (2013).

[8] R. F. Frindt, Single crystals of MoS_2 several molecular layers thick, J. Appl. Phys. **37,** 1928 (1966).

[9] Valeria Nicolosi, Manish Chhowalla, Mercouri G. Kanatzidis, Michael S. Strano, and Jonathan N. Coleman, Liquid exfoliation of layered materials, Science **340,** 1226419 (2013).

[10] Per Joensen, R. F. Frindt, and S. Roy Morrison, Single-layer MoS_2, Mater. Res. Bull. **21,** 457 (1986).

[11] Zhiyuan Zeng, Zongyou Yin, Xiao Huang, Hai Li, Qiyuan He, Gang Lu, Freddy Boey, and Hua Zhang, Single-layer semiconducting nanosheets: High-yield preparation and device fabrication, Angew. Chem. Int. Edit. **50,** 11093 (2011).

[12] Zhiyuan Zeng, Ting Sun, Jixin Zhu, Xiao Huang, Zongyou Yin, Gang Lu, Zhanxi Fan, Qingyu Yan, Huey Hoon Hng, and Hua Zhang, An effective method for the fabrication of few-layer-thick inorganic nanosheets, Angew. Chem. Int. Edit. **51,** 9052 (2012).

[13] Ting Cao, Gang Wang, Wenpeng Han, Huiqi Ye, Chuanrui Zhu, Junren Shi, Qian Niu, Pingheng Tan, Enge Wang, Baoli Liu, and Ji Feng, Valley-selective circular dichroism of monolayer molybdenum disulphide, Nat. Commun. **3,** 887 (2012).

[14] Hualing Zeng, Junfeng Dai, Wang Yao, Di Xiao, and Xiaodong Cui, Valley polarization in MoS_2 monolayers by optical pumping, Nat. Nano. **7,** 490 (2012).

[15] Kin Fai Mak, Keliang He, Jie Shan, and Tony F. Heinz, Control of valley polarization in monolayer MoS_2 by optical helicity, Nat. Nano **7,** 494 (2012).

[16] Kin Fai Mak, Changgu Lee, James Hone, Jie Shan, and Tony F. Heinz, Atomically Thin MoS_2: A new Direct-Gap Semiconductor, Phys. Rev. Lett. **105,** 136805 (2010).

[17] Humberto R. Gutiérrez, Nestor Perea-López, Ana Laura Elías, Ayse Berkdemir, Bei Wang, Ruitao Lv, Florentino López-Urías, Vincent H. Crespi, Humberto Terrones, and Mauricio Terrones, Extraordinary room-temperature photoluminescence in triangular WS_2 monolayers, Nano Lett. **13,** 3447 (2013).

[18] Xiaobo Yin, Ziliang Ye, Daniel A. Chenet, Yu Ye, Kevin O'Brien, James C. Hone, and Xiang Zhang, Edge nonlinear optics on a MoS_2 atomic monolayer, Science **344,** 488 (2014).

[19] Andrea Splendiani, Liang Sun, Yuanbo Zhang, Tianshu Li, Jonghwan Kim, Chi-Yung Chim, Giulia Galli, and Feng Wang, Emerging photoluminescence in monolayer MoS_2, Nano Lett. **10,** 1271 (2010).

[20] Simone Bertolazzi, Jacopo Brivio, and Andras Kis, Stretching and breaking of ultrathin MoS_2, ACS Nano **5,** 9703 (2011).

[21] B. Radisavljevic, A. Radenovic, J. Brivio, V. Giacometti, and A. Kis, Single-layer MoS_2 transistors, Nat. Nano **6,** 147 (2011).

[22] Jonathan N. Coleman *et al.*, Two-dimensional nanosheets produced by liquid exfoliation of layered materials, Science **331,** 568 (2011).

[23] Kai-Ge Zhou, Nan-Nan Mao, Hang-Xing Wang, Yong Peng, and Hao-Li Zhang, A mixed-solvent strategy for efficient exfoliation of inorganic graphene analogues, Angew. Chem. Int. Edit. **50,** 10839 (2011).

[24] Minoru Osada and Takayoshi Sasaki, Exfoliated oxide nanosheets: New solution to nanoelectronics, J. Mater. Chem. **19,** 2503 (2009).

[25] Martin B. Dines, Lithium intercalation via *n*-butyllithium of the layered transition metal dichalcogenides, Mater. Res. Bull. **10,** 287 (1975).

[26] Goki Eda, Hisato Yamaguchi, Damien Voiry, Takeshi Fujita, Mingwei Chen, and Manish Chhowalla, Photoluminescence from chemically exfoliated MoS_2, Nano Lett. **11,** 5111 (2011).

[27] Qing Hua Wang, Kourosh Kalantar-Zadeh, Andras Kis, Jonathan N. Coleman, and Michael S. Strano, Electronics and optoelectronics of two-dimensional transition metal dichalcogenides, Nat. Nanotechnol. **7,** 699 (2012).

[28] A. Castellanos-Gomez, M. Barkelid, A. M. Goossens, V. E. Calado, H. S. J. van der Zant, and G. A. Steele, Laser-thinning of MoS_2: On demand generation of a single-layer semiconductor, Nano Lett. **12,** 3187 (2012).

[29] Wei-Qiang Han, Lijun Wu, Yimei Zhu, Kenji Watanabe, and Takashi Taniguchi, Structure of chemically derived mono- and few-atomic-layer boron nitride sheets, Appl. Phys. Lett. **93,** 223103 (2008).

[30] Yi Lin, Tiffany V. Williams, and John W. Connell, Soluble, exfoliated hexagonal boron nitride nanosheets, J. Phys. Chem. Lett. **1,** 277 (2010).

[31] Graeme Cunningham, Mustafa Lotya, Clotilde S. Cucinotta, Stefano Sanvito, Shane D. Bergin, Robert Menzel, Milo S. P. Shaffer, and Jonathan N. Coleman, Solvent exfoliation of transition metal dichalcogenides: Dispersibility of exfoliated nanosheets varies only weakly between compounds, ACS Nano **6,** 3468 (2012).

[32] Z. Ding, L. Viculis, J. Nakawatase, and R. B. Kaner, Intercalation and solution processing of bismuth telluride and bismuth selenide, Adv. Mater. **13,** 797 (2001).

[33] H. S. S. Ramakrishna Matte, A. Gomathi, Arun K. Manna, Dattatray J. Late, Ranjan Datta, Swapan K. Pati, and C. N. R. Rao, MoS_2 and WS_2 analogues of graphene, Angew. Chem. Int. Edit. **49,** 4059 (2010).

[34] S. Jiménez Sandoval, D. Yang, R. F. Frindt, and J. C. Irwin, Raman study and lattice dynamics of single molecular layers of MoS₂, Phys. Rev. B **44,** 3955 (1991).

[35] Rabin Bissessur, Joy Heising, Wakgari Hirpo, and Mercouri Kanatzidis, Toward pillared layered metal sulfides. intercalation of the chalcogenide clusters $Co_6Q_8(PR_3)_6$ (q = s, se, and te and r = alkyl) into MoS₂, Chem. Mater. **8,** 318 (1996).

[36] Gabin Yoon, Dong-Hwa Seo, Kyojin Ku, Jungmo Kim, Seokwoo Jeon, and Kisuk Kang, Factors affecting the exfoliation of graphite intercalation compounds for graphene synthesis, Chem. Mater. **27,** 2067 (2015).

[37] Reza Rasuli and Azam Irajizad, Density functional theory prediction for oxidation and exfoliation of graphite to graphene, Appl. Surf. Sci. **256,** 7596 (2010).

[38] Gregorio Garcia, Mert Atilhan, and Santiago Aparicio, In silico rational design of ionic liquids for the exfoliation and dispersion of boron nitride nanosheets, Phys. Chem. Chem. Phys. **18,** 1212 (2016).

[39] Yoshiyuki Miyamoto, Hong Zhang, and David Tománek, Photoexfoliation of Graphene from Graphite: An *Ab Initio* Study, Phys. Rev. Lett. **104,** 208302 (2010).

[40] Nina I. Kovtyukhova, Yuanxi Wang, Ayse Berkdemir, Rodolfo Cruz-Silva, Mauricio Terrones, Vincent H. Crespi, and Thomas E. Mallouk, Non-oxidative intercalation and exfoliation of graphite by brønsted acids, Nat. Chem. **6,** 957 (2014), article.

[41] Guijian Guan, Shuangyuan Zhang, Shuhua Liu, Yongqing Cai, Michelle Low, Choon Peng Teng, In Yee Phang, Yuan Cheng, Koh Leng Duei, Bharathi Madurai Srinivasan, Yuangang Zheng, Yong-Wei Zhang, and Ming-Yong Han, Protein induces layer-by-layer exfoliation of transition metal dichalcogenides, J. Am. Chem. Soc. **137,** 6152 (2015).

[42] Jack R. Brent, Nicky Savjani, and Paul O'Brien, Synthetic approaches to two-dimensional transition metal dichalcogenide nanosheets, Prog. Mater. Sci. **89,** 411 (2017).

[43] Xianglu Yin, Yuewei Li, Wei Wu, Guangwen Chu, Yong Luo, and Hong Meng, Preparation of two-dimensional molybdenum disulfide nanosheets by high-gravity technology, Ind. Eng. Chem. Res. **56,** 4736 (2017).

[44] Qingyong Zhang, Liang Mei, Xiehong Cao, Yuxin Tang, and Zhiyuan Zeng, Intercalation and exfoliation chemistries of transition metal dichalcogenides, J. Mater. Chem. A **8,** 15417 (2020).

[45] Liangzhu Zhang, Cheng Chen, Jiadong Zhou, Guoliang Yang, Jiemin Wang, Dan Liu, Zhiqiang Chen, and Weiwei Lei, Solid phase exfoliation for producing dispersible transition metal dichalcogenides nanosheets, Adv. Funct. Mater. **30,** 2004139 (2020).

[46] Giacomo Levita and Maria C. Righi, Effects of water intercalation and tribochemistry on MoS₂ lubricity: An ab initio molecular dynamics investigation (chemphyschem 11/2017), ChemPhysChem **18,** 1490 (2017).

[47] Hyunsoo Lee, Jae-Hyeon Ko, Jin Sik Choi, Jin Heui Hwang, Yong-Hyun Kim, Miquel Salmeron, and Jeong Young Park, Enhancement of friction by water intercalated between graphene and mica, J. Phys. Chem. Lett. **8,** 3482 (2017).

[48] Antonio Cammarata and Tomas Polcar, Control of energy dissipation in sliding low-dimensional materials, Phys. Rev. B **102,** 085409 (2020).

[49] Qionghua Zhou, Qiang Li, Shijun Yuan, Qian Chen, and Jinlan Wang, Band-edge engineering via molecule intercalation: A new strategy to improve stability of few-layer black phosphorus, Phys. Chem. Chem. Phys. **19,** 29232 (2017).

[50] B. Schönfeld, J. J. Huang, and S. C. Moss, Anisotropic mean-square displacements (msd) in single-crystals of 2H- and 3R-MoS₂, Acta Crystallogr. B **39,** 404 (1983).

[51] V. L. Kalikhman, Inorg. Mater. **19,** 957 (1983).

[52] L. H. Brixner, Preparation and properties of the single crystalline AB₂-type selenides and tellurides of niobium, tantalum, molybdenum and tungsten, J. Inorg. Nucl. Chem. **24,** 257 (1962).

[53] W. J. Schutte, J. L. De Boer, and F. Jellinek, Crystal structures of tungsten disulfide and diselenide, J. Solid State Chem. **70,** 207 (1987).

[54] V. L. Kalikhman, Neorganicheskie Materialy **19,** 1060 (1983).

[55] A. A. Yanaki and V. A. Obolonchik, Inorg. Mater. **9,** 1855 (1973).

[56] X. Gonze, G.-M. Rignanese, M. Verstraete, J.-M. Beuken, Y. Pouillon, R. Caracas, F. Jollet, M. Torrent, G. Zerah, M. Mikami, Ph. Ghosez, M. Veithen, J.-Y. Raty, V. Olevano, F. Bruneval, L. Reining, R. Godby, G. Onida, and D. R. Hamann, and D. C. Allan, A brief introduction to the ABINIT software package, Zeitschrift für Kristallographie - Crystalline Materials **220,** 558 (2005).

[57] Marc Torrent, François Jollet, François Bottin, Gilles Zérah, and Xavier Gonze, Implementation of the projector augmented-wave method in the ABINIT code: Application to the study of iron under pressure, Comput. Mater. Sci. **42,** 337 (2008).

[58] X. Gonze *et al.*, ABINIT: First-principles approach to material and nanosystem properties, Comput. Phys. Commun. **180,** 2582 (2009).

[59] X. Gonze *et al.*, Recent developments in the ABINIT software package, Comput. Phys. Commun. **205,** 106 (2016).

[60] Florian Belviso, Antonio Cammarata, Jamil Missaoui, and Tomas Polcar, Effect of electric fields in low-dimensional materials: Nanofrictional response as a case study, Phys. Rev. B **102,** 155433 (2020).

[61] John P. Perdew, Kieron Burke, and Matthias Ernzerhof, Generalized Gradient Approximation Made Simple, Phys. Rev. Lett. **77,** 3865 (1996).

[62] Axel D. Becke and Erin R. Johnson, A simple effective potential for exchange, J. Chem. Phys. **124,** 221101 (2006).

[63] Hendrik J. Monkhorst and James D. Pack, Special points for brillouin-zone integrations, Phys. Rev. B **13,** 5188 (1976).

[64] See Supplemental Material at http://link.aps.org/supplemental/10.1103/PhysRevApplied.15.064041 for section "Geometry of the Z:MX₂ stable structures".

[65] Atsushi Togo and Isao Tanaka, First principles phonon calculations in materials science, Scr. Mater. **108,** 1 (2015).

[66] Laurent Chaput, Atsushi Togo, Isao Tanaka, and Gilles Hug, Phonon-phonon interactions in transition metals, Phys. Rev. B **84,** 094302 (2011).

[67] K. Parlinski, Z. Q. Li, and Y. Kawazoe, First-Principles Determination of the Soft Mode in Cubic ZrO₂, Phys. Rev. Lett. **78,** 4063 (1997).

[68] Antonio Cammarata and Tomas Polcar, Layering effects on low frequency modes in n-layered MX₂ transition

metal dichalcogenides, Phys. Chem. Chem. Phys. **18**, 4807 (2016).

[69] Antonio Cammarata and Tomas Polcar, Vibrational contributions to intrinsic friction in charged transition metal dichalcogenides, Nanoscale **9**, 11488 (2017).

[70] D. M. Wallace, *Thermodynamics of Crystals* (John Wiley & Sons Inc, United States of America, 1972).

[71] J. M. Ziman, *Electrons and Phonons: The Theory of Transport Phenomena in Solids* (Oxford University Press, London, 2001).

[72] J. Safko, H. Goldstein and C. Poole, *Classical Mechanics* (Pearson Education, New York, 2002) 3rd ed. p. 238.

[73] Antonio Cammarata and Tomáš Polcar, Tailoring nanoscale friction in MX_2 transition metal dichalcogenides, Inorg. Chem. **54**, 5739 (2015).

[74] Antonio Cammarata and Tomas Polcar, Overcoming nanoscale friction barriers in transition metal dichalcogenides, Phys. Rev. B **96**, 085406 (2017).

[75] Antonio Cammarata, Paolo Nicolini, Kosta Simonovic, Egor Ukraintsev, and Tomas Polcar, Atomic-scale design of friction and energy dissipation, Phys. Rev. B **99**, 094309 (2019).

[76] Antonio Cammarata and James M. Rondinelli, Covalent dependence of octahedral rotations in orthorhombic perovskite oxides, J. Chem. Phys. **141**, 114704 (2014).

[77] M. J. Han, C. A. Marianetti, and A. J. Millis, Chemical control of orbital polarization in artificially structured transition-metal oxides: $La_2NiXO_6(X = b, al, ga, in)$ from first principles, Phys. Rev. B **82**, 134408 (2010).

[78] Antonio Cammarata and James M. Rondinelli, Octahedral engineering of orbital polarizations in charge transfer oxides, Phys. Rev. B **87**, 155135 (2013).

[79] Antonio Cammarata and Tomas Polcar, Electro-vibrational coupling effects on "intrinsic friction" in transition metal dichalcogenides, RSC Adv. **5**, 106809 (2015).

[80] Graeme Henkelman, Blas P. Uberuaga, and Hannes Jónsson, A climbing image nudged elastic band method for finding saddle points and minimum energy paths, J. Chem. Phys. **113**, 9901 (2000).

[81] Graeme Henkelman and Hannes Jónsson, Improved tangent estimate in the nudged elastic band method for finding minimum energy paths and saddle points, J. Chem. Phys. **113**, 9978 (2000).

[82] G. Kresse and J. Furthmüller, Efficiency of ab-initio total energy calculations for metals and semiconductors using a plane-wave basis set, Comp. Mater. Sci. **6**, 15 (1996).

[83] G. Kresse and D. Joubert, From ultrasoft pseudopotentials to the projector augmented-wave method, Phys. Rev. B **59**, 1758 (1999).